Magnetic exchange coupling in IrMn/NiFe nanostructures: From the continuous film to dot arrays

F. Spizzo,[1] E. Bonfiglioli,[1] M. Tamisari,[1] A. Gerardino,[2] G. Barucca,[3] A. Notargiacomo,[2] F. Chinni,[1] and L. Del Bianco[4,*]

[1]*Dipartimento di Fisica e Scienze della Terra and CNISM, Università di Ferrara, I-44122 Ferrara, Italy*

[2]*Istituto di Fotonica e Nanotecnologie, CNR, I-00156 Roma, Italy*

[3]*Dipartimento SIMAU, Università Politecnica delle Marche, I-60131 Ancona, Italy*

[4]*Dipartimento di Fisica e Astronomia, Università di Bologna, I-40127 Bologna, Italy*

(Received 17 June 2014; revised manuscript received 28 October 2014; published 6 February 2015)

A comprehensive description of the exchange bias phenomenon in an antiferromagnetic/ferromagnetic IrMn(10 nm)/NiFe(5 nm) continuous film and in arrays of square dots with different sizes (1000, 500, and 300 nm) is presented, which elucidates the temperature dependence of the exchange field H_{ex} and coercivity H_C, in conjunction with spatial confinement effects. To achieve this goal, samples prepared by electron beam lithography and lift-off using dc sputtering were subjected to structural investigations by electron microscopy techniques and to magnetic study, through SQUID and magneto-optic magnetometry measurements coupled to micromagnetic calculations. In particular, we have observed that at $T = 300$ K H_{ex} decreases by reducing the size of the dots and it is absent in the smallest ones, whereas the opposite trend is visible at $T = 10$ K ($H_{ex} \sim 1140$ Oe in the dots of 300 nm). The exchange bias mechanism and its thermal evolution have been explained through an exhaustive phenomenological model, which joins spatial confinement effects with other crucial items concerning the pinning antiferromagnetic phase: the magnetothermal stability of the nanograins forming the IrMn layer (mean size ∼10 nm), assumed as essentially noninteracting from the magnetic point of view; the proven existence of a structurally disordered IrMn region at the interface between the NiFe phase and the bulk of the IrMn layer, with a magnetic glassy nature; and the stabilization of a low-temperature ($T < 100$ K) frozen collective regime of the IrMn interfacial spins, implying the appearance of a length of magnetic correlation among them.

DOI: 10.1103/PhysRevB.91.064410 PACS number(s): 75.75.−c, 75.70.−i, 75.50.Lk

I. INTRODUCTION

It is now largely demonstrated that magnetic systems structured on a nanometric scale (i.e., nanoparticles, nanogranular materials, and nanocrystalline thin films) may exhibit peculiar magnetic properties, generally indicated as disordered magnetism effects, originating from the concomitant presence of topological disorder (in surface, interface, or intercrystallites boundary regions) and competing magnetic interactions, as a consequence of the lack of structural periodicity [1–4]. In particular, the frustration of antiferromagnetic interactions (exchange or superexchange) almost invariably results in the insurgence of a glassy magnetic behavior [5–7]. These effects add up with other magnetic phenomena related to the thermal stability of the magnetization of nanosized magnetic elements against thermal fluctuations (superparamagnetic relaxation) [8]. It is to be expected that this complex mix of magnetic effects play a relevant role also in the behavior of exchange coupled antiferromagnetic (AFM)/ferromagnetic (FM) systems, where the torque action exerted by the interfacial AFM spins on the FM ones brings about the insurgence of an unidirectional exchange anisotropy for the FM magnetization, and then the exchange bias (EB) effect [9]. As a matter of fact, although now some studies on the EB effect assume that the AFM layer consists of noninteracting nanograins, whose magnetothermal behavior rules the pinning action of the AFM spins on the FM moments [10–13], recent investigations have proposed the existence of AFM regions with spin-glass-like magnetic properties at the interface with the FM phase [12,14].

Moreover, since the strategic importance of the EB effect in the technology of magnetoresistive spin valves and tunnel junctions and the increasing demand of miniaturization of modern devices (magnetic sensors, high-density data storage media) [15], it is admittedly crucial to expand the description of the EB mechanism so as to include the effects of spatial confinement, namely what happens passing from a continuous AFM/FM film to a nanodot array. In the last decade, exchange coupled AFM/FM nanodots with different sizes, shapes, and compositions have been the objects of different research works, but somewhat contradictory results have been reported. In some cases, an enhanced EB effect was measured at room temperature in the dot systems with respect to the continuous film [16–19], whereas the opposite behavior was found in other cases [20–22]. Baltz *et al.* reported that the effect could be either enhanced or reduced in sub-100 nm soft-FM/AFM dots, with respect to the continuous film, by varying the AFM layer thickness [23]. Only a few studies have addressed the thermal evolution of the EB properties in nanodots [24–28].

Thus, it appears that a complete understanding of the AFM/FM exchange coupling in nanodots has not been achieved yet. In particular, what is still lacking is a comprehensive study of the EB phenomenon in AFM/FM nanodots assessing and elucidating the interplay among the effects of magnetic thermal (in)stability of the AFM nanograins, the magnetothermal evolution of the glassy AFM interfacial regions (characterized by the onset of a frozen collective regime below a critical temperature), and the spatial confinement.

This is the item we have addressed in this research work, dealing with the EB properties of the IrMn/NiFe system in

*Corresponding author: lucia.delbianco@unibo.it

the form of continuous film and of arrays of square dots with different size (1000, 500, and 300 nm), produced by e-beam lithography and lift-off using dc-sputtering deposition. Structural analyses by electron microscopy techniques and magnetic measurements on the continuous bilayer have elucidated the mechanism of interface exchange coupling, especially the role of the AFM IrMn layer, and its dependence on temperature (5–400 K). Then, magnetic measurements on the dot arrays, combined to micromagnetic simulations, have allowed us to comprehend the consequences of spatial confinement on this mechanism.

II. EXPERIMENT

The fabrication of the dot arrays was designed in order to guarantee same processing conditions for all the patterns. Different dot arrays, each one occupying an area of the order of $(100 \times 100)\ \mu m^2$, were patterned on the very same substrate of naturally oxidized Si(100): square dots with size 1000 nm (interdot distance 300 nm), 500 nm (interdot distance 300 nm), and 300 nm (interdot distance 100 nm), which have been labeled as *A*, *B*, and *C*, respectively. Moreover, a single squared structure with size of 500 μm, named as *Q*, was patterned on the substrate to be used as a reference continuous film.

The patterns were exposed by e-beam lithography at 100 kV, on a PMMA bilayer with different molecular weight in order to ease the lift-off process, and developed in MIBK : IPA = 1:3 for 1 min. Then, the deposition process was carried out by dc-magnetron sputtering: in our apparatus it is possible to move the substrate holder so that it is in front of the target source of the material to be grown, so as to have a flux of atoms that is perpendicular to the substrate. Moreover, the apparatus allows the rotation of the substrate guaranteeing a uniform thickness of the sample and it is equipped with a collimator with a 2:1 (height:width) aspect ratio to reduce the angular spread of the incident sputtered atoms [29] (in this way, it is about 10 deg). We have verified that the use of such a collimator greatly favors the lift-off process and offsets the shadow effect, which may alter the dot thickness at the border. The sample was grown in a 0.5 Pa Ar atmosphere and in the presence of a static magnetic field, $H_{dep} = 400$ Oe. The atomic composition of the AFM and FM targets was $Ir_{25}Mn_{75}$ and $Ni_{80}Fe_{20}$, respectively.

The stacking of the final patterns was Si/Cu(5 nm)/IrMn (10 nm)/NiFe(5 nm) (in parentheses the nominal thickness of each layer is reported). The thickness of the layers was determined after calibrating the sputtering sources with a quartz microbalance. After sputtering deposition, the lift-off process was performed using Nano Remover at 80 °C and sonication.

The fabricated dots were analyzed by scanning electron microscopy (SEM). A typical image is displayed in Fig. 1, which refers to the *C* array. The dots appear well separated and regularly distributed. Atomic force microscopy observations confirmed the SEM results and indicated that the dots thickness was consistent with the nominal one (20 nm) within an uncertainty of 10%, irrespective of the dot size. Moreover, the atomic force microscopy analysis confirmed the good degree of thickness uniformity of the dots: a small thickness decrease (at most, 2–3 nm) was found to affect just a very narrow region at the outer border of some dots (namely, the dot profile did not appear squared but slightly rounded).

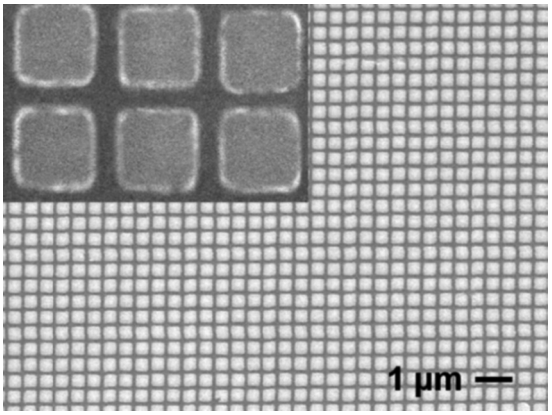

FIG. 1. Typical SEM image of the IrMn/NiFe square dots. In particular, a portion of the array of dots with size of 300 nm is shown (the inset is an enlarged view).

The magnetic properties of the dot arrays were investigated using longitudinal magneto-optic Kerr effect (MOKE) magnetometry with the polarization modulation technique. The MOKE apparatus was equipped with a cryostat allowing us to span the 10–300 K temperature range. The measurements were performed focusing the He-Ne laser light, so as to probe one array of dots at a time.

A continuous film, with the same layer structure as in the dots, was grown by sputtering in identical experimental conditions, in order to have a second reference sample suitable for magnetic measurements by a superconducting quantum interference device (SQUID) magnetometer (operating in the 5–400 K temperature interval). Moreover, a Si/Cu(5 nm)/NiFe(5 nm) sample was also prepared and measured by SQUID to assess the effects on the magnetic properties of the coupling with the IrMn phase.

A portion of the IrMn/NiFe continuous film was employed to carry out transmission electron microscopy (TEM) analysis. The sample was prepared using a dual-beam focused ion beam (FIB) [30]. In order to protect the sample surface during FIB processing, two Pt:C thin films obtained from a metallorganic precursor were deposited, by means of *in situ* deposition processes induced by an electron beam (∼50 nm thick) and subsequently by an ion beam (∼1 μm thick), respectively. A slice of the material was then milled perpendicularly to the sample surface, extracted, and soldered *in situ* on a TEM half-grid by using a nanomanipulator and ion beam induced deposition. The lamella was then finished by thinning at low-voltage and low-current focused ion beams at grazing incidence.

TEM observations were performed by a Philips CM200 microscope operating at 200 kV and equipped with a LaB_6 filament and a double tilt holder.

Finally, micromagnetic simulations were performed using the three-dimensional Object Oriented MicroMagnetic Framework (OOMMF) software, which applies the Landau-Lifshitz-Gilbert equation to simulate the spin configuration and compute the energy and magnetization of nanostructures [31].

III. RESULTS AND DISCUSSION

A. Structural and magnetic properties of the IrMn/NiFe continuous film

1. Transmission electron microscopy

TEM images of the continuous IrMn/NiFe film are shown in Fig. 2. In particular, Fig. 2(a) is a general view of the sample and the different layers are indicated. The Cu layer appears crystalline with a thickness of about 5 nm, in perfect agreement with the nominal value. The lateral dimension of the Cu grains varies between 7 and 10 nm. On this layer the IrMn film has grown with a crystalline structure, the lateral size of the grains ranging from 7 to 10 nm. The thickness of the IrMn layer is about 7–8 nm, lower than the nominal one (10 nm).

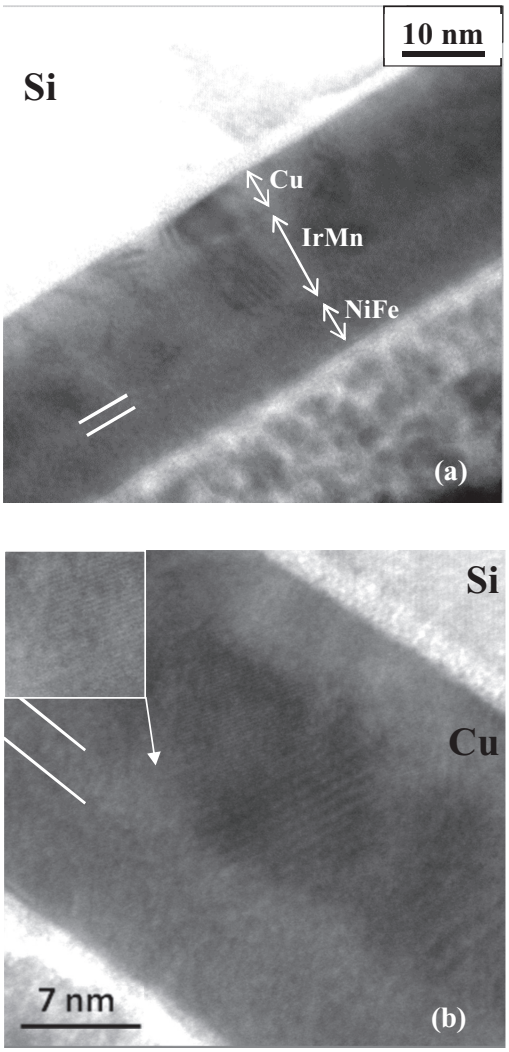

FIG. 2. (a) TEM image of the IrMn/NiFe continuous film. The stack sequence is indicated. The short white lines underline the existence of a thin amorphous region (2–3 nm thick) with a light contrast, located between the IrMn crystalline phase and the amorphous NiFe layer. (b) High resolution image of the sample. The inset in the top-left corner is an enlarged view of a IrMn grain. The parallel white lines are used as in (a).

A final layer, with a thickness of $\sim 7-8$ nm, has been distinguished. In the stacking sequence of the sample, it corresponds to the NiFe film, but the thickness is larger than the nominal one (5 nm). The layer appears amorphous under the electron beam. In particular, the contrast does not change by tilting the sample. The amorphous nature of this layer has been confirmed by high resolution TEM analyses (HRTEM). Different regions of the sample have been imaged, but no crystalline grains have been observed in the upper part of the stack, not even of nanometric size. Figure 2(b) is a typical high resolution image of the sample.

The silicon substrate is in $\langle 110 \rangle$ zone axis orientation and the corresponding atomic positions are visible. An amorphous layer of silicon oxide (1–1.5 nm thick) is visible between the Si substrate and the sputtered sample. The $\{111\}$ atomic planes of IrMn are shown enlarged in the top-left inset of Fig. 2(b): they end at the interface with the amorphous layer in an irregular, topologically disordered way.

As for the amorphous layer, two kinds of contrast are visible in the TEM images, actually. A portion of the amorphous layer, located at the interface with the IrMn phase and having a thickness of 2–3 nm, shows a lighter contrast with respect to the rest of the amorphous phase [it is indicated by parallel white lines in Figs. 2(a) and 2(b)]. In an amorphous material, a different contrast derives from a different thickness of the sample in the electron beam direction or from composition changes. In our case, we exclude that the FIB procedure, employed for the lamella preparation, has produced a detectable variation in the small thickness of the amorphous layer. Therefore, a change in the composition of the amorphous layer near the IrMn interface, with respect to the rest of the upper layer, has to be inferred. It is worth noticing that TEM analyses confirm that the total thickness of the stacking sequence is about 20 nm, in perfect agreement with the nominal one. However, the measured thickness of the crystalline IrMn layer is 2–3 nm smaller than the nominal one, whereas the thickness of the amorphous NiFe is 2–3 nm larger than the nominal one. Hence, considering the different contrasts in the amorphous layer and the thickness of the different films, it is to be concluded that the region of the amorphous layer closer to the crystalline IrMn film is composed of IrMn, actually. This means that an amorphous layer of IrMn is indeed present between the NiFe phase and the crystalline IrMn phase (in the following, we indicate the latter as the "bulk AFM").

2. Magnetic behavior

Hysteresis loops were measured on the IrMn/NiFe continuous film at increasing temperature T after cooling from $T = 300$ K down to $T = 5$ K in a saturating magnetic field $H_{\text{cool}} = 500$ Oe applied along the same direction of H_{dep} during the film deposition.

The loops are shifted to the left along the horizontal field axis, i.e., in the opposite direction to the deposition field. We define the exchange field H_{ex} and the coercivity H_C as positive parameters in this way: $H_{\text{ex}} = -(H_{\text{right}} + H_{\text{left}})/2$ and $H_C = (H_{\text{right}} - H_{\text{left}})/2$, H_{right} and H_{left} being the points where the loop intersects the field axis. The thermal evolution of H_{ex} and H_C is displayed in Fig. 3: both parameters increase with decreasing T, especially at low temperature ($T < 100$ K).

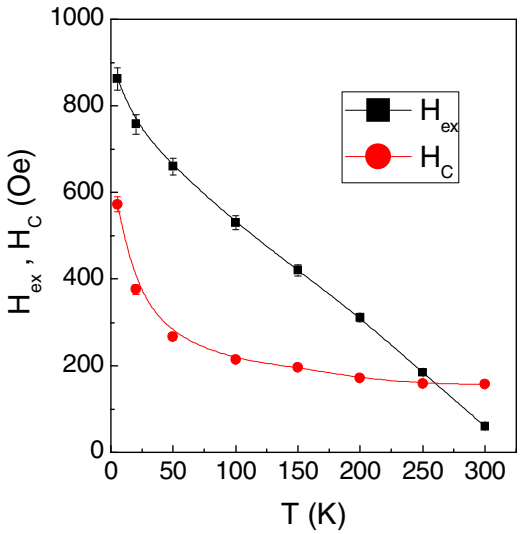

FIG. 3. (Color online) Exchange field H_{ex} (squares) and coercivity H_C (circles) as functions of temperature T (5–300 K) measured by SQUID in the continuous IrMn/NiFe film. In some cases, the error bar is smaller or comparable to the size of the dots. Solid lines are guides to the eye.

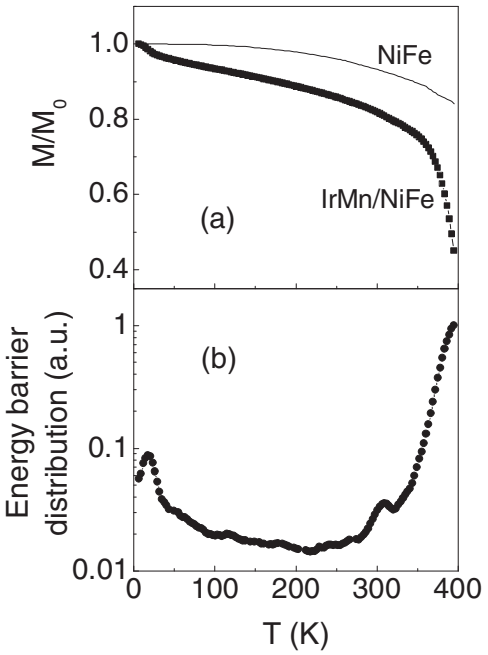

FIG. 4. (a) Magnetization M vs T measured on the continuous IrMn/NiFe film under a magnetic field $H_{inv} = -50$ Oe (full symbols); the thin line is M vs T for the reference NiFe sample, measured in a saturating magnetic field $H = 50$ Oe. Both curves are normalized to the magnetization value at $T = 5$ K, M_0. (b) Distribution of effective anisotropy energy barriers of the IrMn phase (normalized to the peak value) obtained by calculating the temperature derivative of the thick curve in (a), after normalizing to the values of M/M_0 of the thin line in (a). See text for explanation.

This trend is qualitatively similar to what we observed in NiFe/IrMn films [14] despite the different stack configuration (the IrMn layer was on top and the film was capped by a 5-nm-thick Cu layer). In that study, relying exclusively on magnetic results on films with different thickness of IrMn, we proposed a model for the magnetic structure of the AFM phase based on the existence of a disordered region, with a glassy magnetic behavior, interposed between the FM layer and the bulk of the AFM layer; the latter was supposed to consist of nanograins, magnetically independent or weakly interacting [14]. Remarkably, the TEM results shown above definitely confirm our predictions about the structural properties of the AFM phase (Fig. 2), on which the magnetic behavior strictly depends (it is worth reminding that structural disorder is a key ingredient for a spin glass).

We also defined an original protocol for the measurement of the magnetization able to probe the distribution of the anisotropy energy barriers of the AFM phase [14] that was adopted on the continuous film in the present study.

The sample was inserted in the SQUID at room temperature, brought to $T = 400$ K, and cooled down to $T = 5$ K in $H_{cool} = 500$ Oe; then, at $T = 5$ K, a negative magnetic field $H_{inv} = -50$ Oe was applied and the magnetization M was recorded as a function of T.

The curve, normalized to the magnetization value at $T = 5$ K (M_0) is shown in Fig. 4(a) (full symbols) together with the M/M_0 vs T curve (thin line) measured on the reference NiFe film in a saturating magnetic field ($H = 50$ Oe). The marked decrease in the magnetization of the IrMn/NiFe film with temperature is determined by the progressive reduction of the effective magnetic anisotropy acting on the NiFe layer, due to the coupling with IrMn. By calculating the temperature derivative of the IrMn/NiFe curve in Fig. 4(a) (after normalizing to the values of M/M_0 of the thin line, to counterbalance the usual thermal decay of the NiFe magnetization), the figure of the distribution of effective anisotropy energy barriers of the AFM phase is obtained, as sensed by the FM layer. The final result is shown in Fig. 4(b). In agreement with previous findings [14], the AFM entities giving rise to the large peak at high temperature (only partially visible in the present case) are the nanograins in the bulk AFM; below $T \sim 100$ K, the distribution exhibits a tendency to increase slightly and a small peak is well visible at $T \sim 20$ K, which has been associated with the stabilization of a collective frozen regime for the interfacial AFM spins.

Based on these structural and magnetic results, the magnetothermal behavior of the IrMn/NiFe film can be described in the following terms. At $T < 100$ K, the interfacial IrMn spins are frozen in a magnetic glassy state and are collectively involved in the exchange coupling with the NiFe moments. In this condition, the AFM interfacial spins are subjected to a high effective anisotropy and, at $T = 5$ K, H_{ex} and H_C are maximized. In particular, the high H_C—much larger than the value typically measured in NiFe at this temperature (∼20 Oe)—reveals the presence of AFM spins which are dragged by the FM magnetization in the reversal process, probably because they were subjected to a lower local anisotropy within the frozen state. In fact, dragged AFM spins are generally indicated as the primary responsible for the magnetic hardening of the FM phase, often observed in AFM/FM systems [9].

When the collective regime breaks up at $T \sim 100$ K, the orientation of the AFM interfacial spins is determined by the interplay between the magnetic interaction exerted by the FM moments and that exerted by the bulk AFM spins. Only the interfacial AFM spins that are magnetically polarized by those in the bulk AFM and are tightly locked to the lattice of the AFM nanograins are effectively involved in the exchange coupling mechanism (it can be also said that these interfacial spins "re-enter" into the AFM state from the frozen regime, in agreement with the sort of re-entrant ferromagnetic behavior shown by grain boundary spins in nanocrystalline Fe [3]). The AFM interfacial spins polarized by the FM moments, namely those that do not re-enter into the AFM state, will rotate with the FM magnetization and neither will be involved in the EB effect nor will they contribute substantially to H_C. Hence, instead of being ruled by a collectively frozen glassy phase, the exchange coupling is governed by a fraction of interfacial AFM spins, sustained by magnetically uncorrelated AFM nanograins, whose number decreases with increasing temperature, i.e., the thermal energy of the whole system. In fact, a progressive reduction of H_{ex} and H_C is experienced with rising T up to room temperature. At $T = 300$ K, $H_{ex} \sim 60$ Oe: this quite low value indicates that just a small fraction of thermally stable AFM nanograins, able to sustain the EB effect, exists at this temperature. The value of $H_C \sim 160$ Oe at $T = 300$ K, much higher than that of the reference NiFe film (∼5 Oe), still reveals the presence of AFM spins which are dragged by the FM spins during the magnetization reversal. No chance to observe loop shift or H_C enhancement exists at the temperature where all the bulk AFM nanograins are in the superparamagnetic state.

It is worth reminding the x-ray magnetic circular dichroism results reported by Ohldag *et al.* for different exchange bias sandwiches [32]: only a small fraction of the interfacial AFM spins (4%) were tightly locked to the AFM lattice and able to induce the EB effect; most spins rotated in the external field following the FM magnetization reversal. The authors did not fully elucidate the origin of this different behavior of the AFM interfacial spins. In our description, it is a natural consequence of their re-entrant-like behavior. It is to be specified that since our model is based on the assumption that the IrMn layer consists of magnetically noninteracting nanograins (as formerly hypothesized by Fulcomer and Charap [33]), the formation of AFM domain walls, similar to those predicted in the EB models by Mauri [34] and Malozemoff [35], is not considered.

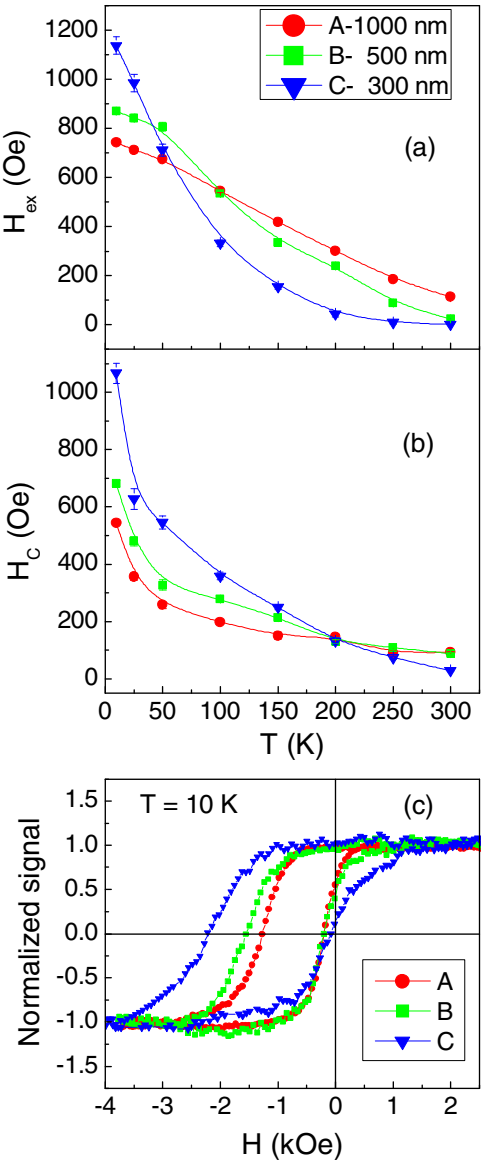

FIG. 5. (Color online) Exchange field H_{ex} (a) and coercivity H_C (b) measured by MOKE as functions of T (10–300 K) on dots A, having size = 1000 nm (circles), dots B with size = 500 nm (squares), and dots C with size = 300 nm (triangles). In some cases, the error bar is smaller or comparable to the size of the symbol. Solid lines are guides to the eye. (c) Hysteresis loops (normalized to the positive saturation value), measured by MOKE at $T = 10$ K on the array of dots A (circles), B (squares), and C (triangles).

B. Exchange bias effect in the dot arrays

Hysteresis loops were measured by MOKE on the arrays of dots in the 10–300 K temperature range after cooling from room temperature in a field $H_{cool} = 500$ Oe. The trends of H_{ex} and H_C with temperature for the reference square Q are in perfect agreement with those in Fig. 3 relative to the continuous film, confirming that the lithography process, in particular the lift-off procedure, did not affect the magnetic properties of the continuous portion of the patterned sample. The curves of H_{ex} and H_C vs T for the dots of type A, B, and C are displayed in Figs. 5(a) and 5(b) [Fig. 5(c) shows the MOKE loops measured on the three arrays of dots at $T = 10$ K]. The behavior of the A dots is not substantially different from that of the square Q and hence of the continuous film (Fig. 3) in the same temperature interval (for this reason, the curves for Q have not been shown).

On the contrary, at $T = 300$ K, H_{ex} is significantly lower in the B array (∼25 Oe) and vanishing in the C one. In all the arrays, H_{ex} increases with decreasing T, but the effect is much more pronounced in the dots with smaller size. Thus, for $T < 100$ K, H_{ex} in B and C dots overcomes that in the A array and at $T = 5$ K the highest H_{ex} is measured in the C dots (∼1140 Oe).

To account for these results we start from our knowledge of the continuous IrMn/NiFe film. We can assume that in

the continuous film, at $T = 300$ K, the interfacial AFM spins giving rise to EB are homogeneously dispersed throughout the interface area. When a patterned area is considered, we can envisage that the same amount of pinning AFM spins is distributed among the dots. If they are very diluted in the continuous film, as reported by Ohldag *et al.* [32], only a few of them will reside in each dot and this number will tend to zero with decreasing dot size. The probability that they are located in the interface region towards the edge of the dot increases with decreasing dot size (in fact, with decreasing the dot size, the total spatial extension of the border regions in the array is enhanced). However, the strength of their pinning action depends on the thermal stability of the AFM grains to which they are anchored. The stability can be reduced in AFM grains located at the dot edge. In fact, their volume is likely to be smaller, compared to that of the grains at the center, because of the spatial confinement that hinders the normal expansion of the grains during the growth process. Moreover, it is certainly to be expected that bulk AFM grains are essentially exchange decoupled, because their size is comparable to the exchange ferromagnetic length of IrMn (∼8 nm) [14]. Nevertheless, the existence of a weak partial coupling between adjacent grains may enhance the thermal stability of those located in the interior of the dot with respect to those at the edge.

In this view, at $T = 300$ K, the very small value of H_{ex} in the *B* dots and the substantial absence of EB in the *C* dots can be accounted for considering that the number of effective AFM pinning centers per dot is too low to cause the insurgence of a strong macroscopic unidirectional anisotropy for the FM magnetization. The enhanced values of H_C (∼90 Oe in *A* and *B* and ∼30 Oe in *C* dots), compared to that of the NiFe layer at room temperature, are consistent with the interfacial AFM spins rotating with the FM magnetization.

With decreasing *T* from 300 K, the thermal stability of the AFM phase improves more and more and this implies that the polarizing action of the bulk AFM grains on the interfacial spins gets stronger and that the number of interfacial spins able to act as pinning centers for the FM magnetization, as well as their efficiency, gets larger. Therefore, both H_{ex} and H_C increase in a percentage much larger for the smaller dots (Fig. 5). Moreover, as the temperature $T = 100$ K is approached (schematically indicated as the temperature that marks the passage to the frozen regime for the interfacial spins), magnetic interaction among interfacial spins must be taken into account.

According to the description given by Mydosh for a canonical spin glass, when the freezing temperature is approached from higher *T*, clusters of interacting spins develop out from the collection of paramagnetic spins [36]. These clusters are characterized by a correlation length λ which rigidly couples together spins pointing along random anisotropy directions under the action of competitive magnetic interactions. Thus, the correlation length increases progressively with reducing *T*. The onset of the glassy state for the interfacial AFM spins, and hence the insurgence of a strong effective anisotropy, explains the observed increase in H_{ex} at low temperature ($T < 100$ K). This last effect is more clearly visible as the dot size is reduced, which indicates that correlated AFM spins exert a stronger pinning action on the FM magnetization as the ratio between the dot size and the correlation length tends to unity. The hypothesis that the EB effect in nanostructures is governed by a characteristic dimension, corresponding to correlated regions in the AFM layer, has been recently reported also by Laureti *et al.* [24]. Although the authors state that the AFM grains are exchange decoupled, in order to account for the EB properties in different sets of Co/CoO nanodots they invoke the existence of a correlation length that may vary with the geometrical and structural features of the dots (thickness of the Co layer and oxidation degree). We unambiguously identify this critical length with the correlation length among the AFM spins of the interfacial spin-glass-like region.

It should be noted that, in principle, in a canonical spin glass the correlation length becomes infinite when the fully glassy state is finally established [36]. Thus, we would expect that at $T = 10$ K, H_{ex} tends to the same value in all the arrays. This is not experimentally observed, actually [Fig. 5(a)]. This can be ascribed to the fact that the interface region is inherently inhomogeneous, both from the structural and magnetic point of view, implying that an infinite correlated glassy state is not established at $T = 10$ K. Moreover, during the loop measurement for determining H_{ex}, the application of the magnetic field (up to 5 kOe) may break up the "infinite" glassy state and limit the extent of the correlation length. A hint of this is the high H_C at very low *T* [Fig. 5(b)] revealing that, despite the high effective anisotropy of the AFM spins in the frozen regime, some of them can still be dragged by the FM moments under a high enough magnetic field.

Hence, at the lowest measuring temperature ($T = 10$ K), the ratio between the dot size and the correlation length will be much closer to unity in dots *C* than in dots *B* and *A*, which accounts for the different H_{ex} values measured at that *T* in the different arrays [Fig. 5(a)].

C. Micromagnetic simulations

In the above description we have substantially distinguished three different temperature regimes: (i) at $T = 300$ K, the number of effective AFM pinning centers is lower in the smaller dots and it may be assumed that the largest possible size of a pinning center corresponds to the mean size of the AFM grains (i.e., ∼10 nm), having considered the AFM grains essentially as noninteracting; (ii) with decreasing *T* down to ∼100 K, the number of effective pinning centers in each dot increases, due to the weakening of thermal effects; and (iii) below $T = 100$ K, magnetic correlations among the AFM interfacial spins are established, which may be depicted as an enlargement of the size of the pinning centers.

In order to support this description, we performed micromagnetic calculations by OOMMF simulating the reversal of the magnetization under an external magnetic field in AFM/FM nanostructures. The OOMMF software is a finite difference code that models a magnetic system using a 3D mesh made of rectangular cells; all the cells have the same size and the magnetization within each cell is supposed to be uniform.

We defined the *x* and *y* axes to be in the plane of the film and the external field to be applied along the *x* direction. In the *x* and *y* directions the size of the cells was of 10 nm, equal to the size of the AFM grains, while in the *z* direction it was of 5 nm, equal to the NiFe layer thickness.

For the NiFe phase, we set the saturation magnetization $M_S = 800\,\text{emu/cm}^3$, stiffness constant $A = 13 \times 10^{-7}\,\text{erg/cm}$, and negligible magnetocrystalline anisotropy. We imposed that, at the beginning of each calculation, the NiFe magnetization was parallel to the applied magnetic field, which is the condition effectively present in a real loop measurement, thanks to the field cooling procedure.

Since the OOMMF code does not allow an antiferromagnetic material to be truly reproduced, the AFM material was simulated by a layer whose magnetocrystalline anisotropy coefficient K_{AFM} and direction d_{AFM} were chosen on a cell basis. The d_{AFM} axes were in the plane of the layer.

The exchange interaction at the AFM/FM interface was assumed to be ferromagnetic and the coupling constant was $A_{\text{ex}} = 10^{-7}\,\text{erg/cm}$.

We were especially interested in verifying our prediction on the variation of H_{ex} with the percentage of pinning centers. For this purpose, a variable percentage p of the AFM cells, uniformly distributed within the system, was given a high K_{AFM} value ($2 \times 10^7\,\text{erg/cm}^3$); d_{AFM} was randomly assigned so as to have a positive projection on the x axis. The high K_{AFM} was set so as to forbid the spin rotation under the external field and, hence, to simulate the presence of blocked AFM grains able to sustain the EB mechanism. A small $K_{\text{AFM}} = 2 \times 10^4\,\text{erg/cm}^3$ was assigned to the remaining cells in order to simulate the existence of AFM grains whose spin lattice easily follows the NiFe magnetization during its reversal. This choice of the K_{AFM} values implies that our simulation does not include AFM spins which are dragged by NiFe spins, hindering the magnetization reversal and affecting H_C. Hence, the values of H_C resulting from the calculations are not of any interest.

The calculations were performed for a dot with size of 1000 nm (A type) and for a dot of 300 nm (C type) and the final H_{ex} values were the average of those obtained over different replicas of the same simulation.

To guarantee homogeneous distributions of the pinning centers inside the dot, the distance between them along x and y was fixed to precise values: according to the adopted scheme, a given distance between the pinning cells resulted in the same p value in A-type and C-type dots.

Actually, the replicas performed for a fixed value of p were calculated changing the relative position of the pinning centers lattice with respect to the dot perimeter. This allowed us to ascertain the absence of any significant dependence of H_{ex} on the specific layout of the pinning centers. In other words, H_{ex} does not depend on the detailed position of the pinning centers, but just on the value of p.

The variation of H_{ex} with the percentage of pinning centers is shown in Fig. 6: H_{ex} increases with increasing the amount of pinning centers, passing from just $\sim$10 Oe, when 1% of pinning centers is present, to a final value larger than 600 Oe. This trend of H_{ex} is very similar in the simulated A and C dots. Hence, as we have proposed, the low H_{ex} measured in the smaller dots at $T = 300\,\text{K}$ [Fig. 5(a)] can be accounted for if one considers that the percentage of effective pinning centers actually reduces with decreasing the dot size. For instance, based on the simulation, the value of H_{ex} measured at $T = 300\,\text{K}$ in the A dots ($\sim$115 Oe) is consistent with a fraction of pinning centers around 10%, whereas the vanishing H_{ex}

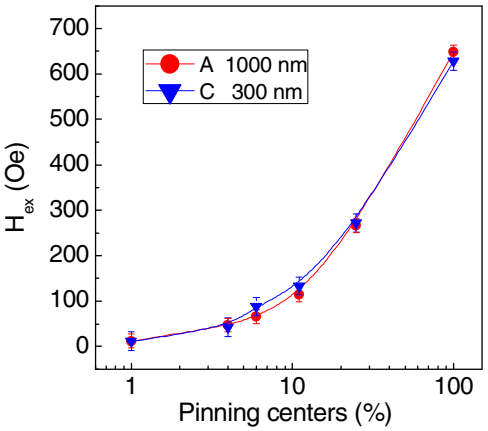

FIG. 6. (Color online) Dependence of H_{ex} on the amount of AFM pinning centers as obtained by micromagnetic calculations simulating the magnetic behavior of a single squared dot with size 1000 nm (A type; circles) and 300 nm (C type; triangles).

in the C dots indicates the presence of a very low amount of effective pinning centers (less than 1%). It is to be noted that these percentages seem quite reasonable, also by the light of the results by Ohldag *et al.* [32]. In concomitance, the results in Fig. 6 also support our statement that the observed increase in H_{ex} with decreasing T from room temperature reflects the increase in the amount of effective pinning centers.

To assess the effect of magnetic correlation among the AFM pinning centers in the low-temperature frozen regime, the following type of simulation was carried out. The situation corresponding to the absence of correlation was simulated dividing the dot into 10 nm squared cells and assigning to each cell $K_{\text{AFM}} = 2 \times 10^7\,\text{erg/cm}^3$ and a d_{AFM} randomly chosen so as to have a positive projection on the x axis. With reference to the results in Fig. 6, this case actually coincides with the simulation for 100% pinning centers. The value of the exchange interaction constant at the AFM/FM interface A_{ex} was the same as before. To simulate the enhancement of λ, the same type of calculation was performed for increasing values of the cell size: 20, 50, 100, 200, and 300 nm [37]. To include also the case of correlation length $\lambda = 300\,\text{nm}$, in all the calculations we have considered a dot size $D = 1200\,\text{nm}$, slightly larger than that of the A dots.

We did not consider larger λ values, closer to D, or smaller dots, despite that these cases would have been very interesting for our study. In fact, when the ratio between λ and D approaches unity, this simulation method does not produce reliable results. The ultimate reason for this is the inherent difficulty of modeling a glassy magnetic structure, featuring a collection of spins subjected to an effective local anisotropy (randomly changing in magnitude and direction on a spatial scale comparable or even shorter than the AFM grain size) and to competing magnetic interactions. In the specific case of the IrMn/NiFe system, the configuration of the frozen interfacial AFM spins must also minimize the exchange interaction energy with the spins of both the NiFe phase and of the AFM grains. In this respect, also the choice of A_{ex} is an oversimplification, since a fixed positive value was used instead of a distribution of exchange coupling constants,

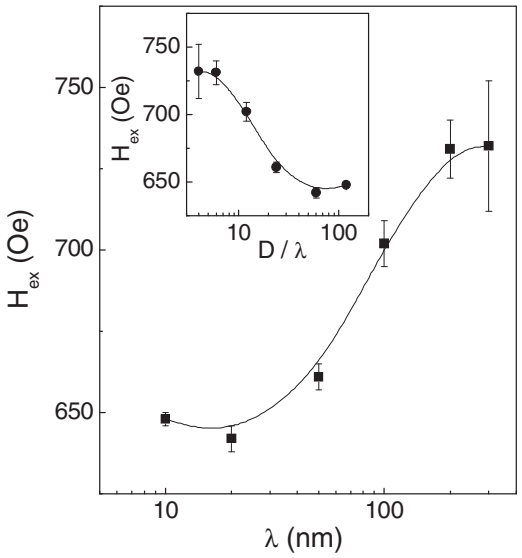

FIG. 7. Dependence of H_{ex} on the length λ of magnetic correlation among AFM pinning centers as obtained by micromagnetic calculations simulating the magnetic behavior of a squared dot with size $D = 1200$ nm. In the inset H_{ex} is plotted as a function of the ratio D/λ.

likely to originate from the interface structural disorder [38]. However, the main problems are connected to the modeling of the magnetic anisotropy. If λ/D is small (namely, the pinning layer is composed of a large number of cells), the random and local character of the magnetic anisotropy of the glassy interfacial phase can be reproduced by our simulation method to a good extent. On the contrary, as λ approaches *D,* the pinning layer is partitioned in just a few cells and the random and local character of the anisotropy is progressively and inevitably lost.

The result of the simulation is shown in Fig 7: H_{ex} increases significantly as the size of the correlated regions grows from 10 to 300 nm (from ∼650 to ∼730 Oe), indicating a trend which is coherent with our expectation (also in this case the H_{ex} values are the average of those obtained over different replicas of the same simulation). The inset of Fig. 7 is the plot of H_{ex} as a function of the ratio between the dot size and the correlation length (D/λ): It illustrates at a glance the concept that H_{ex} increases as D/λ approaches 1. Indeed, we consider the dot of 1200 nm as a model system, where our micromagnetic simulations can be reliably applied to gain unambiguous information on the dependence of H_{ex} on the glassy correlation length. Hence, a trend qualitatively similar of H_{ex} vs D/λ is expected to be observed also in dots of different size.

Finally, we have also calculated the case $\lambda = 1200$ nm, which provides the highest H_{ex} value (980 Oe). Although this result may appear coherent with our prediction, actually it is factitious and for this reason it has not been reported in Fig. 7. In fact, in this calculation we have forced the anisotropy of the pinning layer to stay parallel to the initial NiFe magnetization direction. However, if a perpendicular orientation were imposed, no loop shift would be observed.

IV. CONCLUSIONS

The mechanism of magnetic exchange coupling and its dependence on spatial confinement in the IrMn/NiFe system have been elucidated by studying the thermal evolution of H_{ex} and H_C in a continuous thin film and in arrays of square dots with size varying from 1000 down to 300 nm.

Structural investigations by TEM on a lamella of the continuous IrMn/NiFe film indicate that the bulk of the AFM layer consists of nanograins with mean size ∼10 nm, whereas the NiFe phase appears amorphous. In particular, the TEM analysis definitely reveals the existence of a structurally disordered IrMn region (2–3 nm thick) at the interface between the FM phase and the bulk of the AFM layer.

This finding, namely the evidence of structural disorder, strongly supports our statement about the spin-glass-like magnetic character of the interfacial IrMn region, based on SQUID measurements on the continuous film (Fig. 4). The existence of a low temperature frozen collective regime of the interfacial AFM spins and its break up above a critical temperature, that we have schematically settled at $T = 100$ K, determine the thermal evolution of the EB properties. In fact, below 100 K, the exchange coupling between IrMn and NiFe is ruled by magnetically correlated, frozen AFM spins, subjected to a strong effective local anisotropy, which results in high H_{ex} and H_C values. Above 100 K, the AFM/FM coupling is governed by a fraction of interfacial AFM spins, magnetically polarized by the AFM nanograins. Hence, H_{ex} and H_C decrease more and more with rising T, reflecting the progressive thermal instability of the AFM nanograins, assumed as essentially noninteracting.

The spatial confinement, namely the passage from the continuous film to the dot structure, affects the exchange coupling mechanism when the dot size enters the submicron regime (Fig. 5). In particular, at $T = 300$ K, the low H_{ex} in *B* dots and the absence of EB in *C* dots indicate a decrease in the amount of effective AFM pinning centers with reducing the dot size that we have ultimately ascribed to the worse thermal stability of the AFM nanograins at the dot edge. Since the stability of AFM nanograins improves with decreasing T, determining an increase in the number of AFM pinning centers and in the strength of their pinning action, H_{ex} and H_C increase accordingly, in a percentage much larger for the smaller dots. The marked enhancement of H_{ex} and H_C at low temperature (below 100 K)—visible in all the samples (film and dots), but especially relevant in *C* dots—reflects the progressive freezing of the AFM interfacial spins, whose torque action on the FM moments becomes stronger as the length of magnetic correlation among them increases with reducing T.

To confirm this model, we carried out two different types of simulations. The first one (Fig. 6) confirms the H_{ex} enhancement with increasing the percentage of AFM pinning centers (the size of pinning centers was assumed to coincide with the mean size of the AFM nanograins, i.e., 10 nm). The second simulation shows the tendency of H_{ex} to increase with increasing the correlation length among the AFM pinning centers (Fig. 7). Hence, these simulations provide a strong support to our description, although it is worth noticing that both the increase in the number of effective AFM pinning centers and the expansion of the correlation length are likely

to occur simultaneously when $T = 100$ K is approached from higher T and then with further reducing T down to 10 K.

In conclusion, by combining lithographic methods and sputtering deposition, structural and magnetic results through different techniques, and micromagnetic calculations, we have succeeded in achieving an exhaustive description of the thermal evolution of the EB properties in the IrMn/NiFe system, fully accounting for spatial confinement effects.

ACKNOWLEDGMENTS

This research work was sponsored by MIUR under project FIRB2010 'Tailoring the magnetic anisotropy of nanostructures for enhancing the magnetic stability of magnetoresistive devices - NANOREST'. Dr. D. Bisero and Dr. S. Fin (University of Ferrara, Italy) are acknowledged for carrying out the atomic force microscopy analysis.

[1] R. H. Kodama, A. E. Berkowitz, E. J. McNiff, and S. Foner, Phys. Rev. Lett. **77**, 394 (1996).

[2] B. Martinez, X. Obradors, Ll. Balcells, A. Rouanet, and C. Monty, Phys. Rev. Lett. **80**, 181 (1998).

[3] E. Bonetti, L. Del Bianco, D. Fiorani, D. Rinaldi, R. Caciuffo, and A. Hernando, Phys. Rev. Lett. **83**, 2829 (1999).

[4] Z. Sefrioui, J. L. Menéndez, E. Navarro, A. Cebollada, F. Briones, P. Crespo, and A. Hernando, Phys. Rev. B **64**, 224431 (2001).

[5] L. Del Bianco, F. Boscherini, A. L. Fiorini, M. Tamisari, F. Spizzo, M. V. Antisari, and E. Piscopiello, Phys. Rev. B **77**, 094408 (2008).

[6] E. Winkler, R. D. Zysler, M. Vasquez Mansilla, and D. Fiorani, Phys. Rev. B **72**, 132409 (2005).

[7] A. Hernando, E. Navarro, M. Multigner, A. R. Yavari, D. Fiorani, M. Rosenberg, G. Filoti, and R. Caciuffo, Phys. Rev. B **58**, 5181 (1998).

[8] J. L. Dormann, D. Fiorani, and E. Tronc, Adv. Chem. Phys. **98**, 283 (1997).

[9] J. Nogués, J. Sort, V. Langlais, V. Skumryev, S. Suriñach, J. S. Muñoz, and M. D. Barò, Phys. Rep. **422**, 65 (2005).

[10] M. Molina-Ruiz, A. F. Lopeandía, F. Pi, D. Givord, O. Bourgeois, and J. Rodríguez-Viejo, Phys. Rev. B **83**, 140407(R) (2011).

[11] G. Vallejo-Fernandez, T. Deakin, K. O'Grady, S. Oh, Q. Leng, and M. Pakala, J. Appl. Phys. **107**, 09D709 (2010).

[12] V. Baltz, B. Rodmacq, A. Zarefy, L. Lechevallier, and B. Dieny, Phys. Rev. B **81**, 052404 (2010).

[13] T. R. Gao, D. Z. Yang, S. M. Zhou, R. Chantrell, P. Asselin, J. Du, and X. S. Wu, Phys. Rev. Lett. **99**, 057201 (2007).

[14] F. Spizzo, M. Tamisari, E. Bonfiglioli, and L. Del Bianco, J. Phys.: Condens. Matter **25**, 386001 (2013).

[15] C. Chappert, A. Fert, and F. N. Van Dau, Nat. Mater. **6**, 813 (2007).

[16] A. Nemoto, Y. Otani, S. G. Kim, K. Fukamichi, O. Kitakami, and Y. Shimada, Appl. Phys. Lett. **74**, 4026 (1999).

[17] K. Liu, S. M. Baker, M. Tuominen, T. P. Russell, and I. K. Schuller, Phys. Rev. B **63**, 060403(R) (2001).

[18] M. Tofizur Rahman, N. N. Shams, D. S. Wang, and C.-H. Lai, Appl. Phys. Lett. **94**, 082503 (2009).

[19] G. García, M Kiwi, J. Mejía-López, and R. Ramírez, J. Magn. Magn. Mater. **322**, 3329 (2010).

[20] M. Fraune, U. Rüdiger, G. Güntherodt, S. Cardoso, and P. Freitas, Appl. Phys. Lett. **77**, 3815 (2000).

[21] Y. Shen, Y. Wu, H. Xie, K. Li, J. Qiu, and Z. Guo, J. Appl. Phys. **91**, 8001 (2002).

[22] V. Baltz, J. Sort, B. Rodmacq, B. Dieny, and S. Landis, Appl. Phys. Lett. **84**, 4923 (2004).

[23] V. Baltz, J. Sort, S. Landis, B. Rodmacq, and B. Dieny, Phys. Rev. Lett. **94**, 117201 (2005).

[24] S. Laureti, S. Y. Suck, H. Haas, E. Prestat, O. Bourgeois, and D. Givord, Phys. Rev. Lett. **108**, 077205 (2012).

[25] V. Baltz, G. Gaudin, P. Somani, and B. Dieny, Appl. Phys. Lett. **96**, 262505 (2010).

[26] G. Vallejo-Fernandez and J. N. Chapman, J. Appl. Phys. **107**, 09D704 (2010).

[27] J. Eisenmenger, Z.-P. Li, W. A. A. Macedo, and I. K. Schuller, Phys. Rev. Lett. **94**, 057203 (2005).

[28] V. Baltz, J. Sort, B. Rodmacq, B. Dieny, and S. Landis, Phys. Rev. B **72**, 104419 (2005).

[29] J. Cook, Thin Solid Films **338**, 81 (1999).

[30] J. Mayer, L. A. Giannuzzi, T. Kamino, and J. Michael, MRS Bull. **32**, 400 (2007).

[31] M. J. Donahue and D. G. Porter, in *OOMMF User's Guide, Version 1.0 Interagency Report NISTIR 6376* (National Institute of Standards and Technology, Gaithersburg, MD, 1999).

[32] H. Ohldag, A. Scholl, F. Nolting, E. Arenholz, S. Maat, A. T. Young, M. Carey, and J. Stöhr, Phys. Rev. Lett. **91**, 017203 (2003).

[33] E. Fulcomer and S. H. Charap, J. Appl. Phys. **43**, 4190 (1972).

[34] D. Mauri, H. C. Siegmann, P. S. Bagus, and E. Kay, J. Appl. Phys. **62**, 3047 (1987).

[35] A. P. Malozemoff, Phys. Rev. B **35**, 3679 (1987).

[36] J. A. Mydosh in *Spin glasses: An Experimental Introduction* (Taylor and Francis, London, 1993).

[37] When we addressed the dependence of H_{ex} on λ, we made preliminary calculations using cells with size of 10 nm (the correlation among the AFM cells was simulated by imposing to them the same direction of K_{AFM}). In this case we noticed that, as λ was increased, also the NiFe magnetic configuration displayed a similar correlation length. To assess if this effect depended on the choice of the cell size, we performed calculations changing the value of the latter. The results obtained by the two methods were perfectly consistent. Hence, we decided to show in the paper only those obtained by the second approach since, in our opinion, the change in the spin-glass correlation length is schematically better represented by increasing the size of the cells.

[38] J. M. D. Coey, J. Appl. Phys. **49**, 1646 (1978).